Pressure-induced emission enhancement with an abnormal blue shift of the Sb³⁺-doped zero-dimensional lead-free halide perovskite Cs₂InBr₅ · H₂O

Jiaxiang Wang,[1,*] Yifang Yuan,[1,*] Cailong Liu,[2] Ruijing Fu,[3] Lingrui Wang ®,[1,†] Fei Zhang,[1] Liang Ma,[1]
Sheng Jiang,[4] Zhifeng Shi,[1,‡] and Haizhong Guo ®[1,5,§]

[1]*Key Laboratory of Material Physics, Ministry of Education, School of Physics and Microelectronics,
Zhengzhou University, Zhengzhou 450052, People's Republic of China*
[2]*Shandong Key Laboratory of Optical Communication Science and Technology, School of Physics Science
Information Technology, Liaocheng University, Liaocheng 252059, People's Republic of China*
[3]*School of Applied Physics and Materials, Wuyi University, Jiangmen 529020, People's Republic of China*
[4]*Shanghai Advanced Research Institute, Chinese Academy of Sciences, Shanghai 201210, People's Republic of China*
[5]*Institute of Quantum Materials and Physics, Henan Academy of Sciences, Zhengzhou 450046, People's Republic of China*

Zero-dimensional (0D) lead-free halide perovskites doped with ns^2-metal ions have emerged as an interesting research topic, due to their broad luminescence spectra and large Stokes shift for both fundamental research and future optoelectronic applications. Herein, we report an abnormal phenomenon of pressure-induced blue-shifted and enhanced emission in Sb³⁺-doped Cs₂InBr₅ · H₂O. The pressure-induced photoluminescence enhancement (<0.6 GPa) of Sb³⁺:Cs₂InBr₅ · H₂O can be ascribed to the less energy difference between $^3P_1$ of Sb³⁺ and self-trapped exciton (STE) state, and the reduced nonradiative energy loss. Meanwhile, the pressure-induced anisotropic contraction of inhomogeneously coordinated $[SbBr_5O]H_2^{2-}/[InBr_5O]H_2^{2-}$ octahedra is highly responsible for the unusual blue-shifted STE emission and the variation of the band gap. These findings provide a basis for understanding the structure-properties correlation of ns^2-metal ions doped 0D perovskite, and shed light on the effects of the pressure in emission enhancement and tuning the optical properties of halide perovskites.

I. INTRODUCTION

Zero-dimensional (0D) lead-free halide perovskites, which consist of electronically isolated metal halide anions and organic ands inorganic cations, are gaining increasing attention in recent years [1]. The interest stems from their excellent optoelectronic properties, such as remarkable ambient stability, large exciton binding energy, and broad-band emission, which promote them widely applied in various optoelectronic devices. Among the reported 0D halide perovskite materials, indium- (In-) based perovskites have been attracting strong attention due to their low toxicity, oxidization avoidance capabilities, and superior luminescence performance [2–5]. Despite these advances, their photoluminescence (PL) efficiency is relatively low due to the small light absorption coefficient corresponding to the excitation region, limiting their further application [6]. In this sense, various strategies have been proposed to improve their optical properties. Doping ns^2-metal ions such as Sb³⁺$(5s^2)$, Te⁴⁺$(5s^2)$, Bi³⁺$(6s^2)$, and Tl⁺$(6s^2)$, etc., in 0D In-based halide perovskites are an effective strategy to improve the emission performance and achieving efficient PL [7–14]. Recently, it has been reported

that Sb³⁺ was compatible with the crystal and able to improve the performance of 0D In-based halide perovskites, owing to the same valence and similar ionic radius as the In³⁺ ions. For example, Chen *et al.* successfully synthesized $A_2InX_5 \cdot H_2O$ and A_3InX_6 $(A = Cs, Rb; X = Cl, Br)$ crystals via $5s^2$-metal Sb³⁺ doping, and the photoluminescence quantum yield (PLQY) of the doped crystals increased dramatically (above 90%) [15]. Crystals with bright orange emission were obtained by Kuang *et al.* by introducing Te⁴⁺ into Cs₂InCl₅ · H₂O. The sensitivity of the $5s^2$ lone pairs of electrons in the Te⁴⁺ ion to temperature was also found, and the Te⁴⁺-doped Cs₂InCl₅ · H₂O has a strong temperature dependence and an easily measurable lifetime [16]. Nonetheless, the origin and mechanism of the emission in the ion-doped perovskites are still debated [17–21]. Therefore, it is important to investigate the structure-optical property relationships of the Sb³⁺-doped 0D In-based halide perovskites in order to improve the photoemission properties, and also to reveal the excited-state dynamics processes of the doped Sb³⁺ ions.

High pressure has been pointed out as an effective approach to access the structure-property relationships, optimize the optical performance, and promote the emergence of novel features [22–27]. In terms of the excited-state dynamics related to material photoemission, high pressures can provide a new dimension to access novel phenomena and structures that are difficult to find at ambient pressures, thus revealing the potential emission mechanism [28–32]. By comparing Mn-doped and undoped Cs₂NaBiCl₆ double perovskites, Zou *et al.*

---

*These authors contributed equally to this work.

†wanglr@zzu.edu.cn

‡shizf@zzu.edu.cn

§hguo@zzu.edu.cn

reported a significant pressure-induced emission enhancement (PIEE) of the former (<0.5 GPa), induced by the overlap of the electronic wave functions and the energy transfer from Bi^{3+} to Mn^{2+} ions [33]. The PIEE phenomena have been also found in Mn^{2+}-doped $CsPbCl_3$ nanocrystals, Eu-doped $CsPbCl_3$ quantum dots, and Mn^{2+}/Cu^{2+}-codoped $CsPbCl_3$, related to the enhanced energy transfer rate from the excitonic states to the doped ions [29,34,35]. From this point of view, it is expected that the optical response of the Sb^{3+}-doped 0D In-based halide perovskites can be enhanced by the pressure.

Therefore, we investigate the changes of the structural and optical properties of $Sb^{3+}:Cs_2InBr_5 \cdot H_2O$ under high pressure. With increasing the pressure, $Sb^{3+}:Cs_2InBr_5 \cdot H_2O$ exhibits a trend of PIEE (<0.6 GPa), then the photoemission intensity gradually decreases and quenches above 11.0 GPa. Intriguingly, the emission peak shows an unusual and persistent blue shift companied by a red-shift absorption band gap throughout the compression process. Meanwhile, the $[SbBr_5O]H_2^{2-}/[InBr_5O]H_2^{2-}$ octahedra undergo considerable distortions through an isostructural phase transition that occurs in the pressure region of 2.7–7.8 GPa. The experimental results reveal the structure-properties relationship of $Sb^{3+}:Cs_2InBr_5 \cdot H_2O$, and provide theoretical guidance for the optimization of the performance and multifunctionality of the ion-doped halide perovskites.

II. METHODS

CsBr (99.9%), $Sb(CH_3CO_2)_3$ (99.9%), HBr (48%) were purchased from Aladdin. $In(CH_3CO_2)_3$ (99.99%) was purchased from Sigma-Aldrich. Methanol (99.5%) was purchased from Macklin. All the chemical reagents were used as received without further purification. The crystal sample of $Sb^{3+}:Cs_2InBr_5 \cdot H_2O$ was synthesized according to the procedure described in previous reports [15]. The Sb^{3+} acts as the dopant ion by replacing the position of In^{3+} in the host $Cs_2InBr_5 \cdot H_2O$, and the molar ratio of In/Sb during synthesis was 93:7 ($Sb^{3+} = 7\%$). A symmetric diamond anvil cell (DAC) and a pair of IIa-type diamond anvils with the culets size of 400 μm were used for the high-pressure measurements. The sample was loaded into a hole of the T301 steel gasket (diameter 150 μm), and the thickness of the gasket indentation was 42 μm. The ruby fluorescence technique was adopted for the pressure calibration, and silicon oil (Aladdin, 10 cst) was applied as pressure-transmitting medium (PTM) around the sample [36].

In situ high-pressure photoluminescence experiments were carried out using a UV DPSS laser with the excitation wavelength of 355 nm (37 μW). The power-dependent PL emission was monitored by a power meter of THORLABS PM100D. It should be noted that the parameters of the excitation light source were fixed during the experiment to avoid its influence on the final photoluminescence intensity of the sample. *In situ* high-pressure absorption spectra were performed using a fiber spectrometer (QE65000, Ocean Optics). *In situ* high-pressure Raman spectra were recorded using a spectrometer equipped with the liquid-nitrogen-cooled CCD (iHR550, Symphony II, Horiba Jobin Yvon). The 532-nm diode laser was used to excite the sample and the output power is 10 mW. *In situ* high-pressure synchrotron ADXRD experiments were conducted

at the BL15U1 beamline of Shanghai and 4W2 High Pressure Station of Beijing Synchrotron Radiation Facility. The experiments were carried out using a monochromatic x-ray beam with a wavelength of 0.6199 Å. The refinement of the XRD pattern was completed using the Reflex module in the MATERIALS STUDIO software. The Pawley profile-fitting routine was first used to refine the cell parameters and search the space group, and then the Rietveld refinement was executed to obtain the crystal structural parameters.

III. RESULTS AND DISCUSSION

A. Emission and absorption

To investigate the optical properties of $Sb^{3+}:Cs_2InBr_5 \cdot H_2O$ under the different pressures, the *in situ* high-pressure PL experiments were carried out. The PL spectra during the compression are shown in Fig. 1(a). As for $Sb^{3+}:Cs_2InBr_5 \cdot H_2O$ under ambient conditions, the PL spectrum exhibits a broad-band orange-red emission centered at 672 nm with a large Stokes shift of 318 nm. Accordingly, these features have been identified as the intrinsic self-trapped excitons (STEs) emission, which depends profoundly on the structure distortion [37]. As previous reported, the broad-band emission is mainly associated with the presence of large octahedral distortion in $Sb^{3+}:Cs_2InBr_5 \cdot H_2O$, and arises from the emission of the Sb^{3+} ions, i.e., the $^3P_1 \rightarrow ^1S_0$ electron leap within the Sb^{3+} ion [15]. The PL intensity gradually increases with increasing the pressure and reaches a maximum value at 0.6 GPa, then decreases with further compression and disappears when the pressure exceeds 11.0 GPa. However, the PL peak of $Sb^{3+}:Cs_2InBr_5 \cdot H_2O$ shows a continuous blue shift during the compression regimes. This PIEE phenomenon with combining an insistent blue-shift PL peak is different from the previous reports, suggesting that $Sb^{3+}:Cs_2InBr_5 \cdot H_2O$ has a unique photoemission mechanism. The variations of the PL intensity, peak position, and the full width at half-maximum (FWHM) with the pressure are clearly demonstrated in Figs. 1(b) and 1(c) and Fig. S1 [38]. All of the three emission state parameters undergo roughly three evolutionary processes, with the emission intensity enhancing until 0.6 GPa (Fig. S2) [38], the peak position and FWHM decreasing rapidly below 2.7 GPa, slowing down from 2.7–7.3 GPa, and remaining essentially constant after 7.9 GPa, which may be related to the structural change of $Sb^{3+}:Cs_2InBr_5 \cdot H_2O$ under the pressure [39]. Ultimately, the PL intensity quenches, which may be caused by the pressure-induced partly amorphization phenomenon [31,39]. The PL peak is observed at 561 nm at around 11.0 GPa, which is 110 nm blue shifted compared with that of ambient pressure. To quantitatively evaluate the evolution of $Sb^{3+}:Cs_2InBr_5 \cdot H_2O$ emission properties, we measured the photoluminescence quantum yield (PLQY) of the material under ambient conditions and based on this we estimated the PLQY at high pressures (Table S1) [38], which is consistent with the experimental results (see also [40,41] therein). The PL intensity of the sample versus the laser power is shown in Fig. S3 [38]. Upon the decompression, the PL returns to the initial state, but the PL intensity decreases (Fig. S4) [38]. And this is closely related to its crystal structure. The corresponding emission color of
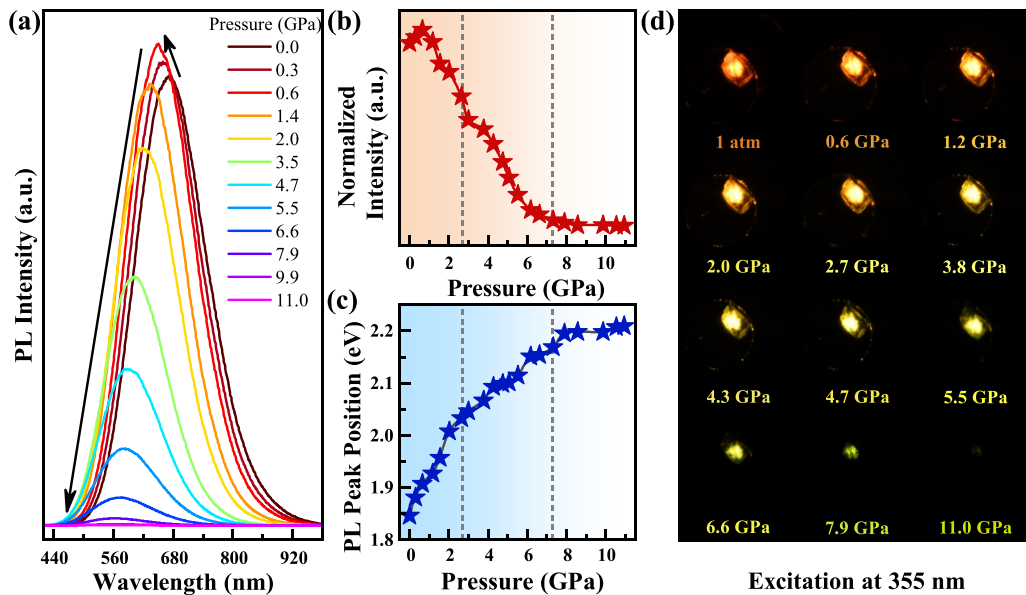
FIG. 1. Pressure-induced evolutions of (a) the PL spectra, (b) the normalized PL intensity, (c) the PL peak position, and (d) the PL micrographs (irradiated with 355 nm constant power laser) of Sb^{3+}:$Cs_2InBr_5 \cdot H_2O$. The black arrows represent the evolution of the PL peak and intensity under the pressure.

Sb^{3+}:$Cs_2InBr_5 \cdot H_2O$ under the pressure modulation can be seen in the optical micrographs as illustrated in Fig, 1(d). The emission color undergoes a process from orange-red to yellow to dull green. We also record the Commission Internationale de l'Eclairage (CIE) chromaticity coordinates to visualize the pressure-induced color evolution of Sb^{3+}:$Cs_2InBr_5 \cdot H_2O$ emitted light (Fig. S5) [38]. The CIE chromaticity coordinates vary continuously from (0.60, 0.39) at ambient pressure to (0.41, 0.51) at 11.0 GPa. In general, the dopant ion concentration, energy band structure, and structural transition affect the emission properties of halide perovskite materials [15,22]. In order to exclude the effect of Sb^{3+}-doping concentration on the evolution of the emission behavior of the material under high pressure and to verify the pressure-induced emission enhancement phenomenon, we also prepared a series of Sb^{3+}:$Cs_2InBr_5 \cdot H_2O$ with different molar ratios (Sb^{3+} = 1%, 5%, and 10%). As shown in Fig. S6 [38], the PL spectra of all three samples (1%, 5%, and 10%) exhibit pressure-induced emission enhancement phenomena analogously. And the PL spectra of all samples show similarly continuous blue shift with their intensity increasing and then decreasing, and finally disappearing. Thus, we excluded the influence of the dopant ion concentration on the trend of the emission evolution of the material at high pressures and on this basis we selected the samples with the same dopant ion concentration (7%) for the further experiments.

The tuning of the optical properties of the materials under the pressure is closely related to the alteration of the electronic structure. *In situ* high-pressure UV-Vis absorption experiments of up to 20.5 GPa were performed in order to understand the unique optical properties of Sb^{3+}:$Cs_2InBr_5 \cdot H_2O$. As shown in Fig. 2(a), there are two absorption modes in the system at ambient conditions, which are represented here by the high- and low-energy absorption modes. For the

high-energy absorption part (edge 1), it is mainly attributed to the electron leap from the valence band maximum of the main body $Cs_2InBr_5 \cdot H_2O$ (consisting of the $4p$ orbital of Br and the $5s$ orbital of In) to the conduction band minimum (mainly contributed by the $5p$ orbital of In); for the low-energy absorption part (edge 2), it is caused by the $^1S_0 \rightarrow {}^3P_1$ leap
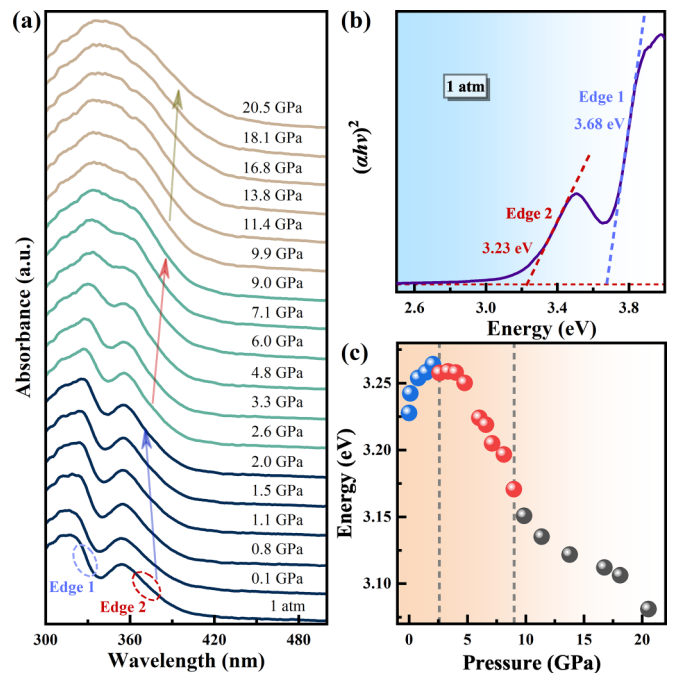

FIG. 2. (a) The UV-Vis absorption spectra of Sb^{3+}:$Cs_2InBr_5 \cdot H_2O$ as a function of pressure; (b) the Tauc plot under ambient conditions; (c) the variation of band gap with pressure of Sb^{3+}:$Cs_2InBr_5 \cdot H_2O$.
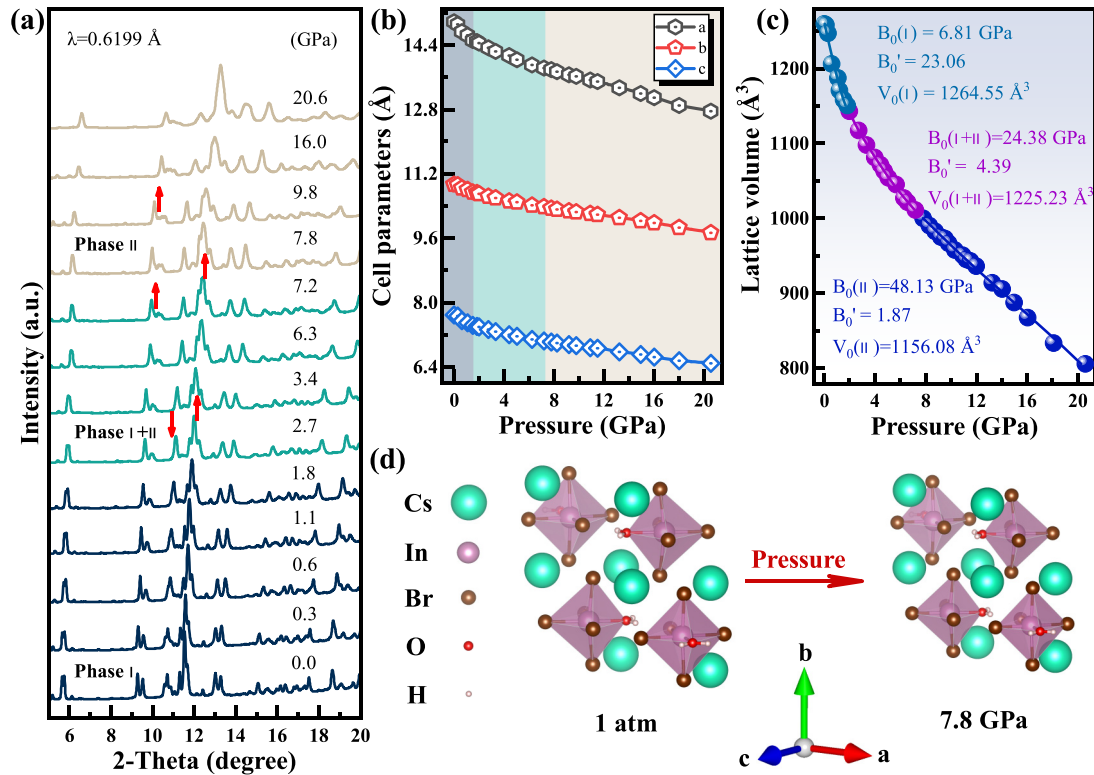
FIG. 3. (a) The ADXRD spectra of Sb^{3+}:$Cs_2InBr_5 \cdot H_2O$ compressed to 20.6 GPa. The cell parameters (b) lattice constant and (c) cell volume of Sb^{3+}:$Cs_2InBr_5 \cdot H_2O$ with pressure. (d) Structural diagram at 1 atm and 7.8 GPa.

of the Sb^{3+} ion in the isolated $[SbBr_5O]H_2^{2-}$ octahedron. By analyzing the energy difference between edges 1 and 2, we find that the energy difference between the two different absorption parts decreases with increasing the pressure (Fig. S7) [38]. With increasing the pressure, the absorption edge of Sb^{3+}:$Cs_2InBr_5 \cdot H_2O$ first undergoes a slight blue shift, i.e., the absorption edge moves towards to the higher energy. Beyond 2.6 GPa, the absorption edge shows a gradual red shift. After 7.2 GPa, the energy difference between the two different energy-absorbing sides shows a negative value. This implies that it becomes easier for the energy to transfer from the main body to the dopant ion guest during the pressurization. At 9.0 GPa, the two separate absorbing edges move together and the red-shift rate with the pressure slows down. Upon the decompression, the absorption spectrum is almost the same as that before the pressure treatment, with slightly different intensities, as shown in Fig. S8 [38]. The optical band-gap values of Sb^{3+}:$Cs_2InBr_5 \cdot H_2O$ are obtained by extrapolating the intersection of the $(\alpha h\nu)^2$ linear part against $h\nu$ in the Tauc diagram, where α is the absorption coefficient and $h\nu$ is the photon energy [Fig. 2(b)]. The evolution of the band gap with the pressure can be seen in Fig. 2(c). The band-gap value increases slightly from 3.23 eV at ambient pressure to 3.26 eV at 2.0 GPa, followed by a rapid decrease with further increasing the pressure. Throughout the experiment, the sample obtained a minimum optical band-gap value of 3.08 eV at 20.5 GPa. This pressure modulation of the band gap indicates that the pressure can effectively tune the optical absorption and photoemission properties of the ion-doped 0D halide perovskites system.

B. Structural analysis

Based on the previous findings of the high-pressure tuned structure-properties relationships of the halide perovskites, there is a close relationship between their optical properties and the internal inorganic octahedral units. Two abrupt changes in the absorption spectra of Sb^{3+}:$Cs_2InBr_5 \cdot H_2O$ and the anomalous photoluminescence spectra suggest that the material may have undergone structural changes associated with the changes in the electronic structure. Based on this, *in situ* high-pressure angle-dispersive x-ray diffraction (ADXRD) and Raman experiments were carried out with the applied pressure to investigate the structural behaviors of Sb^{3+}:$Cs_2InBr_5 \cdot H_2O$ [Figs. 3(a) and S9] [38]. It is observed that the introduction of Sb^{3+} did not lead to the appearance of new diffraction peaks (Table S2) [38] (see also Ref. [42] therein). According to the Rietveld refinement (Fig. S10) [38], Sb^{3+}:$Cs_2InBr_5 \cdot H_2O$ crystallizes in the orthorhombic phase with a space group *Pnma* (phase I) under ambient condition, yielding a slight increase in the lattice constants [phase I, space group: *Pnma*, $a = 14.977(1)$ Å, $b = 10.930(3)$ Å, and $c = 7.695(2)$ Å] compared to the host $Cs_2InBr_5 \cdot H_2O$ due to the ionic radius of Sb^{3+} that in the central octahedral larger than that of the In^{3+} ion. With increasing the pressure to 2.7 GPa, the overall diffraction peaks move towards to the higher diffraction angles, implying the pressure-induced lattice contraction of the orthorhombic phase, as also evidenced by the Raman vibration modes shifting continuously to the higher frequencies. At 2.7 GPa, the peak at around 11° disappears and a new peak appears at around 12°, indicating a transition occurs from the orthorhombic phase to a new

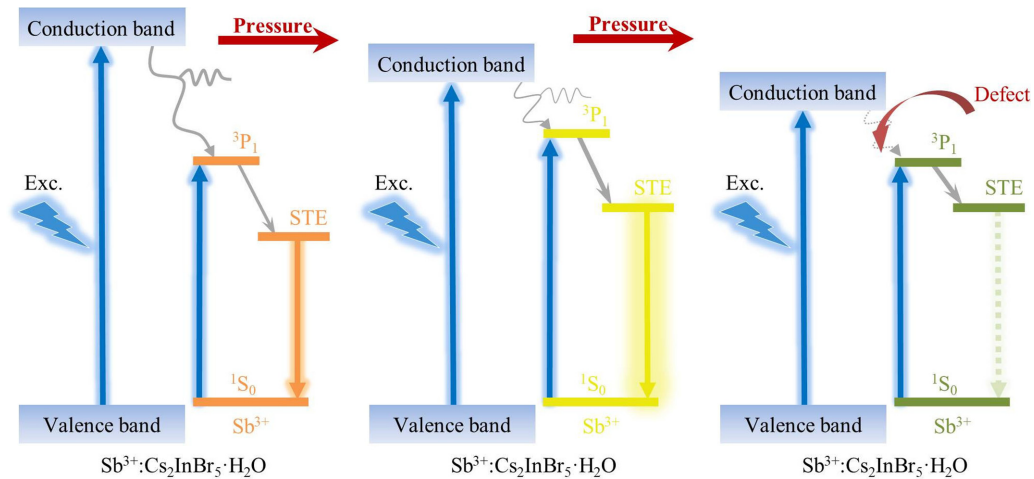FIG. 4. Schematic illustrations of emission mechanism evolutions of Sb^{3+}:$Cs_2InBr_5 \cdot H_2O$ upon lattice compression.

phase. After compression to 7.2 GPa, the crystal structure is completely transformed into the new phase as the new diffraction peak moves out at around $10°$ (Figs. S11 and S12) [38]. Moreover, the splitting and appearance of the Raman vibration mode in this pressure region indicate that the phase transition is related to the variation of the $[SbBr_5O]H_2^{2-}$/$[InBr_5O]H_2^{2-}$ octahedra. The Rietveld refinement shows that the space group of the high-pressure new phase at 7.8 GPa (phase II, space group: *Pnma*, lattice parameters: $a = 13.786(3)$ Å, $b = 10.336(8)$ Å, and $c = 7.018(3)$ Å) adopts the same structural symmetry with the initial orthorhombic phase. Upon the compression to 20.6 GPa, both the ADXRD and Raman spectra show that the peaks are broadened, indicating that phase II begins to undergo a structural amorphization process. Sb^{3+}:$Cs_2InBr_5 \cdot H_2O$ has a similar phase transition path as that of the host material $Cs_2InBr_5 \cdot H_2O$ under the pressure.

In addition, the parameters of the lattice constant and cell volume with the pressure as shown in Figs. 3(b) and 3(c), respectively. During the structural evolution, the cell shrinks faster along the c-axis direction, while the b-axis direction has the strongest resistance to the compression. Hence, the cell parameters of Sb^{3+}:$Cs_2InBr_5 \cdot H_2O$ exhibit obvious anisotropic contraction. As shown in Figs. S13– S15 [38], the contraction is anisotropic at all three stages with increasing pressure, which is related to the inhomogeneous coordination environment of the inorganic octahedra and the deformation under pressure. From the structural viewpoint, the phenomenon may be related to the inhomogeneous coordination environment of the $[SbBr_5O]H_2^{2-}$/$[InBr_5O]H_2^{2-}$ octahedra and the directionality of the hydrogen bonding within the surrounding octahedral units [Fig. 3(d)] [22]. In order to clarify the behavior of the inorganic octahedra during structural evolution, the bond lengths and bond angles of the $[InBr_5O]H_2^{2-}$ octahedra were analyzed (Figs. S16– S18) [38]. Furthermore, the pressure-volume data are here fitted with the third-order Birch-Murnaghan equation of state, and the processed results are shown in Fig. 3(c) (see also Ref. [43] therein). In phase I, the bulk modulus (B_0) of Sb^{3+}:$Cs_2InBr_5 \cdot H_2O$ after fitting is 6.81 GPa, smaller than that of the conventional 3D perovskite $MAPbI_3$ (13.6 GPa), indicating that Sb^{3+}:$Cs_2InBr_5 \cdot H_2O$ has a strong structural tunability under the pressure. The B_0 values

for the coexistence phase (phase I + phase II) and phase II are 24.38 and 48.13 GPa, respectively. The higher B_0 indicates higher stability under the pressure, which is closely related to the special hydrogen bonding network structure inside the main body.

C. Mechanism

Through the above analysis, we can conclude that there is relevance between the PL responses of Sb^{3+}:$Cs_2InBr_5 \cdot H_2O$ and the lattice variations. According to previous reports, the wide emission with the large Stokes shift originated from STEs is mainly a result of the strong electron-phonon coupling and transient elastic lattice distortions under an excited state [37]. The pressure-regulated exciton-phonon coupling can be quantified using Huang-Rhys factor S. According to the relationship between the Stokes displacement energy E_{Stokes} and optical branch phonon modes ($E_{Stokes} = 2S\hbar\omega_{LO}$), the evolution trend of the S factor with the pressure is obtained (Figs. S19 and S20) [38,44]. The intrinsic STE emissions of Sb^{3+}:$Cs_2InBr_5 \cdot H_2O$ are understood as follows in Fig. 4. At ambient conditions, we obtained a large Huang-Rhys parameter of 20.2, which exhibits giant electron-phonon coupling via Fröhlich interaction in the Sb^{3+}:$Cs_2InBr_5 \cdot H_2O$ crystal. The broad-band emission is contributed by the strong electron-phonon coupling. The parameter S decreases monotonously as the pressure increases, indicating the decrease in the electron-phonon coupling strength reduced by the lattice compression. According to the energy gap law, the energy difference between the initial and final states decreases, reducing nonradiative loss. Meanwhile, FWHM of the STE emission decreases as the pressure increases, reflecting the decrease of the lattice relaxation energy and the energy difference between multiple STEs. Such changes result in the band-gap narrowing and STE enhancement of Sb^{3+}:$Cs_2InBr_5 \cdot H_2O$ under mild compression (<0.6 GPa). With further increasing the pressure, the structure of Sb^{3+}:$Cs_2InBr_5 \cdot H_2O$ exhibits obvious anisotropic contraction, leading to an increase of the defects and the nonradiative recombination, therefore, the PL intensity decreases. And the rapid attenuation of the PL strength can be attributed to the rapid increase of

the defects in the system caused by the structural phase transition.

During compression, the S factor of the system gradually decreases, which indicates that the strength of the electron-phonon coupling of the material is weakened, i.e., the self-trapped excitons cannot be stabilized, leading to a reduction in the emission of the system. However, the enhancement of the system emission suggests that the STE emission here is not part of the system's intrinsic STE emission. Rather, it is the STE state associated with the Sb^{3+} ion. The weakening of the emission due to the lifting of the STE state and the reduction of the S factor competes with the increase in energy transfer due to the reduction of the energy difference between the host and the object and the reduction in energy loss, and these two mechanisms together lead to an increase in the overall emission intensity of the system. The first-principles density functional theory (DFT) calculations show that the high-pressure phase exhibits an increased electronic band dispersion compared to the ambient phase (Figs. S21a and S21b) [38] (see also Refs. [45–50] therein), allowing for easier energy transfer between host (In) and guest (Sb). Additionally, the broadening of the exciton energy level associated with Sb poses a challenge in forming stable self-trapped excitons that are dependent on Sb. These two competing mechanisms influence the system during the pressurization process, providing a plausible explanation for the observed behavior of initially increasing and then decreasing emission intensity [51].

IV. CONCLUSION

In summary, we have investigated the intrinsic structure-property relationships of Sb^{3+}:$Cs_2InBr_5 \cdot H_2O$ under the pressure, and an abnormal phenomenon of the pressure-induced blue-shifted and enhanced STE emission is achieved. During the pressurization, the structure of Sb^{3+}:$Cs_2InBr_5 \cdot H_2O$ shows an obvious anisotropic contraction due to the inhomogeneous coordination environment of $[SbBr_5O]H_2^{2-}$/$[InBr_5O]H_2^{2-}$ octahedra. Such structural variation is directly related to the high-pressure behavior of the STE emission. The enhanced emission in the lower-pressure range of 0–0.6 GPa is associated with increased energy transfer between the host and object. The evolution of the emission intensity and peak position at high pressure suggests that the broad-band emission originates from the STE state associated with the Sb^{3+} ion. This work deepens the understanding of the correlation between structural and optical properties of the Sb^{3+}:$Cs_2InBr_5 \cdot H_2O$, and provides experimental evidence and theoretical guidance for the elucidation of the dynamics of the excited states of Sb^{3+}, thus promoting the application of such materials.

[1] S. Sun, M. Lu, X. Gao, Z. Shi, X. Bai, W. W. Yu, and Y. Zhang, 0D perovskites: Unique properties, synthesis, and their applications, Adv. Sci. **8**, 2102689 (2021).

[2] J.-W. Lee, S. Tan, S. I. Seok, Y. Yang, and N.-G. Park, Rethinking the A cation in halide perovskites, Science **375**, eabj1186 (2022).

[3] L. Zhu, H. Cao, C. Xue, H. Zhang, M. Qin, J. Wang, K. Wen, Z. Fu, T. Jiang, L. Xu *et al.*, Unveiling the additive-assisted oriented growth of perovskite crystallite for high performance light-emitting diodes, Nat. Commun. **12**, 5081 (2021).

[4] Y. Liu, Z. Li, J. Xu, Y. Dong, B. Chen, S. M. Park, D. Ma, S. Lee, J. E. Huang, S. Teale *et al.*, Wide-bandgap perovskite quantum dots in perovskite matrix for sky-blue light-emitting diodes, J. Am. Chem. Soc. **144**, 4009 (2022).

[5] Z. Liu, W. Qiu, X. Peng, G. Sun, X. Liu, D. Liu, Z. Li, F. He, C. Shen, Q. Gu *et al.*, Perovskite light-emitting diodes with EQE exceeding 28% through a synergetic dual-additive strategy for defect passivation and nanostructure regulation, Adv. Mater. **33**, 2103268 (2021).

[6] X. Liu, X. Xu, B. Li, Y. Liang, Q. Li, H. Jiang, and D. Xu, Antimony-doping induced highly efficient warm-white emission in indium-based zero-dimensional perovskites, CCS Chemistry **2**, 216 (2020).

[7] G. Wu, R. Liang, M. Ge, G. Sun, Y. Zhang, and G. Xing, Surface passivation using 2D perovskites toward efficient and stable perovskite solar cells, Adv. Mater. **34**, 2105635 (2022).

[8] D. Cui, X. Liu, T. Wu, X. Lin, X. Luo, Y. Wu, H. Segawa, X. Yang, Y. Zhang, Y. Wang *et al.*, Making room for growing oriented $FASnI_3$ with large grains via cold precursor solution, Adv. Funct. Mater. **31**, 2100931 (2021).

[9] D. Chen, F. Dai, S. Hao, G. Zhou, Q. Liu, C. Wolverton, J. Zhao, and Z. Xia, Crystal structure and luminescence properties of lead-free metal halides $(C_6H_5CH_2NH_3)_3MBr_6$ (M = Bi and Sb), J. Mater. Chem. C **8**, 7322 (2020).

[10] R. Zhang, X. Mao, Y. Yang, S. Yang, W. Zhao, T. Wumaier, D. Wei, W. Deng, and K. Han, Air-stable, lead-free zero-dimensional mixed bismuth-antimony perovskite single crystals with ultra-broadband emission, Angew. Chem. Int. Ed. **58**, 2725 (2019).

[11] S. Liu, B. Yang, J. Chen, D. Wei, D. Zheng, Q. Kong, W. Deng, and K. Han, Efficient thermally activated delayed

fluorescence from all-inorganic cesium zirconium halide perovskite nanocrystals, Angew. Chem. Int. Ed. **59**, 21925 (2020).

[12] B.-B. Zhang, J.-K. Chen, J.-P. Ma, X.-F. Jia, Q. Zhao, S.-Q. Guo, Y.-M. Chen, Q. Liu, Y. Kuroiwa, C. Moriyoshi *et al.*, Antithermal quenching of luminescence in zero-dimensional hybrid metal halide solids, J. Phys. Chem. Lett. **11**, 2902 (2020).

[13] P. W. M. Jacobs, Alkali halide crystals containing impurity ions with the ns^2 ground-state electronic configuration, J. Phys. Chem. Solids **52**, 35 (1991).

[14] Z. Tan, Y. Chu, J. Chen, J. Li, G. Ji, G. Niu, L. Gao, Z. Xiao, and J. Tang, Lead-free perovskite variant solid solutions $Cs_2Sn_{1-x}Te_xCl_6$: Bright luminescence and high anti-water stability, Adv. Mater. **32**, 2002443 (2020).

[15] X. Cheng, R. Li, W. Zheng, D. Tu, X. Shang, Z. Gong, J. Xu, S. Han, and X. Chen, Tailoring the broadband emission in all-inorganic lead-free 0D in-based halides through Sb^{3+} doping, Adv. Opt. Mater. **9**, 2100434 (2021).

[16] J.-H. Wei, J.-B. Luo, J.-F. Liao, W.-T. Ou, and D.-B. Kuang, Te^{4+}-doped $Cs_2InCl_5 \cdot H_2O$ single crystals for remote optical thermometry, Sci. China Mater. **65**, 764 (2022).

[17] J. Xu, S. Li, C. Qin, Z. Feng, and Y. Du, Identification of singlet self-trapped excitons in a new family of white-light-emitting zero-dimensional compounds, J. Phys. Chem. C **124**, 11625 (2020).

[18] J. Zhang, Y. Yang, H. Deng, U. Farooq, X. Yang, J. Khan, J. Tang, and H. Song, High quantum yield blue emission from lead-free inorganic antimony halide perovskite colloidal quantum dots, ACS Nano **11**, 9294 (2017).

[19] Z. Ma, Z. Shi, D. Yang, F. Zhang, S. Li, L. Wang, D. Wu, Y. Zhang, G. Na, L. Zhang *et al.*, Electrically-driven violet light-emitting devices based on highly stable lead-free perovskite $Cs_3Sb_2Br_9$ quantum dots, ACS Energy Lett. **5**, 385 (2020).

[20] J. Pal, S. Manna, A. Mondal, S. Das, K. V. Adarsh, and A. Nag, Colloidal synthesis and photophysics of $M_3Sb_2I_9$ (M = Cs and Rb) nanocrystals: Lead-free perovskites, Angew. Chem. Int. Ed. **56**, 14187 (2017).

[21] Z. Tan, M. Hu, G. Niu, Q. Hu, J. Li, M. Leng, L. Gao, and J. Tang, Inorganic antimony halide hybrids with broad yellow emissions, Sci. Bull. **64**, 904 (2019).

[22] L. Wang, P. Yao, F. Wang, S. Li, Y. Chen, T. Xia, E. Guo, K. Wang, B. Zou, and H. Guo, Pressure-induced structural evolution and bandgap optimization of lead-free halide double perovskite $(NH_4)_2SeBr_6$, Adv. Sci. **7**, 1902900 (2020).

[23] Z. Ma, Q. Li, J. Luo, S. Li, L. Sui, D. Zhao, K. Yuan, G. Xiao, J. Tang, Z. Quan *et al.*, Pressure-driven reverse intersystem crossing: New path toward bright deep-blue emission of lead-free halide double perovskites, J. Am. Chem. Soc. **143**, 15176 (2021).

[24] T. Yamauchi, T. Shimazu, D. Nishio-Hamane, and H. Sakurai, Contrasting Pressure-Induced Metallization Processes in Layered Perovskites, α-Sr_2MO_4 (M = V, Cr), Phys. Rev. Lett. **123**, 156601 (2019).

[25] D. Zhao, G. Xiao, Z. Liu, L. Sui, K. Yuan, Z. Ma, and B. Zou, Harvesting cool daylight in hybrid organic-inorganic halides microtubules through the reservation of pressure-induced emission, Adv. Mater. **33**, 2100323 (2021).

[26] J. Wang, L. Wang, Y. Li, R. Fu, Y. Feng, D. Chang, Y. Yuan, H. Gao, S. Jiang, F. Wang *et al.*, Pressure-induced metallization

[27] L. Ma, K. Wang, Y. Xie, X. Yang, Y. Wang, M. Zhou, H. Liu, X. Yu, Y. Zhao, H. Wang *et al.*, High-Temperature Superconducting Phase in Clathrate Calcium Hydride CaH_6 up to 215 K at a Pressure of 172 GPa, Phys. Rev. Lett. **128**, 167001 (2022).

of lead-free halide double perovskite $(NH_4)_2PtI_6$, Adv. Sci. **9**, 2203442 (2022).

[28] H. Luo, S. Guo, Y. Zhang, K. Bu, H. Lin, Y. Wang, Y. Yin, D. Zhang, S. Jin, W. Zhang *et al.*, Regulating exciton-phonon coupling to achieve a near-unity photoluminescence quantum yield in one-dimensional hybrid metal halides, Adv. Sci. **8**, 2100786 (2021).

[29] Y. Cao, G. Qi, L. Sui, Y. Shi, T. Geng, D. Zhao, K. Wang, K. Yuan, G. Wu, G. Xiao *et al.*, Pressure-induced emission enhancements of Mn^{2+}-doped cesium lead chloride perovskite nanocrystals, ACS Mater. Lett. **2**, 381 (2020).

[30] R. Li, R. Wang, Y. Yuan, J. Ding, Y. Cheng, Z. Zhang, and W. Huang, Defect origin of emission in $CsCu_2I_3$ and pressure-induced anomalous enhancement, J. Phys. Chem. Lett. **12**, 317 (2021).

[31] Z. Ma, Z. Liu, S. Lu, L. Wang, X. Feng, D. Yang, K. Wang, G. Xiao, L. Zhang, S. A. T. Redfern *et al.*, Pressure-induced emission of cesium lead halide perovskite nanocrystals, Nat. Commun. **9**, 4506 (2018).

[32] D. Samanta, S. P. Chaudhary, B. Ghosh, S. Bhattacharyya, G. Shukla, and G. D. Mukherjee, Pressure-induced emission enhancement and bandgap narrowing: Experimental investigations and first-principles theoretical simulations on the model halide perovskite $Cs_3Sb_2Br_9$, Phys. Rev. B **105**, 104103 (2022).

[33] L. Zhang, Z. Liu, X. Sun, G. Niu, J. Jiang, Y. Fang, D. Duan, K. Wang, L. Sui, K. Yuan *et al.*, Retainable bandgap narrowing and enhanced photoluminescence in Mn-doped and undoped $Cs_2NaBiCl_6$ double perovskites by pressure engineering, Adv. Opt. Mater. **10**, 2101892 (2022).

[34] X. Jing, D. Zhou, R. Sun, Y. Zhang, Y. Li, X. Li, Q. Li, H. Song, and B. Liu, Enhanced photoluminescence and photoresponsiveness of Eu^{3+} ions-doped $CsPbCl_3$ perovskite quantum dots under high pressure, Adv. Funct. Mater. **31**, 2100930 (2021).

[35] J. Zhang, Y. Zheng, G. Liu, Y. Ma, L. Gong, R. Guan, X. Cui, J. Yan, J. Zhao, and J. Yang, Pressure-engineered optical and charge transport properties of Mn^{2+}/Cu^{2+} codoped $CsPbCl_3$ perovskite nanocrystals via structural progression, ACS Appl. Mater. Interfaces **12**, 48225 (2020).

[36] H. K. Mao, J. Xu, and P. M. Bell, Calibration of the ruby pressure gauge to 800 kbar under quasi-hydrostatic conditions, J. Geophys. Res. **91**, 4673 (1986).

[37] M. D. Smith and H. I. Karunadasa, White-Light Emission from Layered Halide Perovskites, Acc. Chem. Res. **51**, 619 (2018).

[38] See Supplemental Material at http://link.aps.org/supplemental/10.1103/PhysRevB.107.214111 for additional figures in support of the data analysis.

[39] Q. Li, B. Xu, Z. Chen, J. Han, L. Tan, Z. Luo, P. Shen, and Z. Quan, Excitation-dependent emission color tuning of 0D $Cs_2InBr_5 \cdot H_2O$ at high pressure, Adv. Funct. Mater. **31**, 2104923 (2021).

[40] K. Rurack, and M. Spieles, Fluorescence quantum yields of a series of red and near-infrared dyes emitting at 600-1000 nm, Anal. Chem. **83**, 1232 (2011).

[41] G. Kleideiter, M. D. Lechner, and W. Knoll, Pressure dependence of thickness and refractive index of thin PMMA-films investigated by surface plasmon and optical waveguide spectroscopy, Macromol. Chem. Phys. **200**, 1028 (1999).

[42] L. Zhou, J.-F. Liao, Z.-G. Huang, J.-H. Wei, X.-D. Wang, W.-G. Li, H.-Y. Chen, D.-B. Kuang, and C.-Y. Su, A highly red-emissive lead-free indium-based perovskite single crystal for sensitive water detection, Angew. Chem. Int. Ed. **58**, 5277 (2019).

[43] M. J. Cliffe and A. L. Goodwin, PASCal: A principal axis strain calculator for thermal expansion and compressibility determination, J. Appl. Crystallogr. **45**, 1321 (2012).

[44] L. Zhang, Y. Fang, L. Sui, J. Yan, K. Wang, K. Yuan, W. L. Mao, and B. Zou, Tuning emission and electron-phonon coupling in lead-free halide double perovskite $Cs_2AgBiCl_6$ under pressure, ACS Energy Lett. **4**, 2975 (2019).

[45] G. Kresse and J. Furthmüller, Efficiency of *ab-initio* total energy calculations for metals and semiconductors using a plane-wave basis set, Comput. Mater. Sci. **6**, 15 (1996).

[46] G. Kresse and J. Furthmüller, Efficient iterative schemes for *ab initio* total-energy calculations using a plane-wave basis set, Phys. Rev. B **54**, 11169 (1996).

[47] P. E. Blöchl, Projector augmented-wave method, Phys. Rev. B **50**, 17953 (1994).

[48] J. P. Perdew, K. Burke, and M. Ernzerhof, Generalized Gradient Approximation Made Simple, Phys. Rev. Lett. **77**, 3865 (1996).

[49] S. Grimme, Semiempirical GGA-type density functional constructed with a long-range dispersion correction, J. Comput. Chem. **27**, 1787 (2006).

[50] A. V. Krukau, O. A. Vydrov, A. F. Izmaylov and G. E. Scuseria, Influence of the exchange screening parameter on the performance of screened hybrid functionals, J. Chem. Phys. **125**, 224106 (2006).

[51] J. Yu, J. Kong, W. Hao, X. Guo, H. He, W. R. Leow, Z. Liu, P. Cai, G. Qian, S. Li *et al.*, Broadband extrinsic self-trapped exciton emission in Sn-doped 2D lead-halide perovskites, Adv. Mater. **31**, 1806385 (2019).